Science and Technology Indonesia
e-ISSN:2580-4391 *p*-ISSN:2580-4405
Vol. 11, No. 3, July 2026

Research Paper

PVA/PVP Dissolving Microneedle Arrays Loaded with *Parameria laevigata* Extract: Formulation and Characterization for Transdermal Anti-Acne Therapy

Angga Saputra Yasir[1*], Siwi Nurbaiti[1], Jenifer Kolina[1], Amalia Lathifah Widiadari[1], Harmiansyah[2,3,4], Muhammad Asyraf Muhammad Rizal[2,3,5], Melbi Mahardika[6]

[1]*Cosmetic Engineering Study Program, Institut Teknologi Sumatera, Lampung, 35365, Indonesia*
[2]*Centre for Advanced Composite Materials (CACM), Universiti Teknologi Malaysia, Johor Bahru, Johor, 81310, Malaysia*
[3]*Department of Applied Mechanics and Design, Faculty of Mechanical Engineering, Universiti Teknologi Malaysia, Johor Bahru, Johor, 81310, Malaysia*
[4]*Department of Biosystem Engineering, Faculty of Industrial Technology, Institut Teknologi Sumatera, Lampung, 35365, Indonesia.*
[5]*Institute of Tropical Forestry and Forest Products (INTROP), Universiti Putra Malaysia, Serdang, Selangor, 43400, Malaysia*
[6]*Research Center for Biomass and Bioproducts, National Research and Innovation Agency (BRIN), Serpong, South Tangerang, 15314, Indonesia*
***Corresponding author**: angga.yasir@km.itera.ac.id

Abstract
Despite the well-documented antimicrobial and antioxidant properties of *Parameria laevigata* (kayu rapet) bark, its incorporation into a dissolving microneedle (DMN) platform for transdermal acne therapy has not been previously investigated. This study developed and characterized PVA/PVP-based DMN arrays loaded with *P. laevigata* extract as a minimally invasive delivery system targeting acne-associated pathogens. Ultrasonic-assisted extraction in 95% ethanol yielded a phytochemical-rich extract (8.68%) containing flavonoids, tannins, saponins, and alkaloids, with strong antioxidant activity (DPPH IC_{50} = 40.98 ± 4.32 ppm; ABTS IC_{50} = 46.92 ± 3.25 ppm; FRAP = 70.24 ± 6.41 mg AAE/g extract) and moderate antibacterial activity against *Staphylococcus aureus* and *Cutibacterium acnes* at 100–150 ppm (inhibition zone: 8.22–8.46 mm). Eight DMN formulations were fabricated at a fixed 30% w/w PVA/PVP total polymer concentration with 5% extract loading. The optimized formulation (F2) produced a complete 49-needle pyramidal array with adequate mechanical integrity for stratum corneum penetration, confirmed polymer–extract physicochemical compatibility by FTIR, and exhibited Korsmeyer–Peppas release kinetics with a diffusion-controlled mechanism reaching 56.48% cumulative release over 24 h. These findings establish *P. laevigata*-loaded DMN arrays as a viable proof-of-concept platform for transdermal acne therapy, warranting further ex vivo permeation and in vivo efficacy validation.

Keywords
Parameria laevigata, Dissolving Microneedle, PVA/PVP Matrix, Transdermal Delivery, Anti-Acne Therapy

Received: 23 March 2026, Accepted: 10 May 2026
https://doi.org/10.26554/sti.2026.11.3.1016-1032

1. INTRODUCTION

Acne (*Acne vulgaris*) is one of the most prevalent global dermatological problems, particularly among adolescents and young adults. Global Burden of Disease data indicated that acne prevalence increased from 8,563.4 per 100,000 population in 1990 to 9,790.5 per 100,000 in 2021, with an annual growth rate of 0.43% (Zhu et al., 2025). In Asia, a study in Malaysia reported a prevalence of 67.5% among the adolescent group (Hanisah et al., 2009). Acne vulgaris is among the most prevalent dermatological conditions in Indonesia, affecting an estimated 85–100% of adolescents and young adults. Peak prevalence has been reported at 83–85% in females aged 14–17 years and 95–100% in males aged 16–19 years (Rimadhani and Rahmadewi, 2015; Saragih et al., 2016). This condition demonstrates that acne is a health issue that requires effective and sustainable management.

Pathophysiologically, acne is triggered by several factors, including excessive sebum production, follicular hyperkeratinization, colonization by *Cutibacterium acnes*, and inflammatory responses that trigger the formation of reactive oxygen species (ROS) (Popa et al., 2023). Increased ROS levels cause oxidative stress that damages cell membranes, lipids, proteins, and DNA, thereby exacerbating inflammation and skin tissue damage (Siddiqui et al., 2024). High oxidative stress also correlates with increased acne severity, characterized by elevated oxidative biomarkers and decreased endogenous antioxidant activity (Balik et al., 2023). Therefore, the use of antioxidant compounds has become an important therapeutic strategy in controlling the inflammatory process in acne.

Various acne therapies have been developed, such as retinoids, benzoyl peroxide, and topical or oral antibiotics, including clindamycin, erythromycin, and doxycycline (Li et al., 2024). However, long-term use of antibiotics potentially causes antimicrobial resistance (Alkhawaja et al., 2020). Resistance to *Cutibacterium acnes* was reported to reach 60.1% for macrolides in Indonesia (Legiawati et al., 2023), while resistance to azithromycin was reported to range between 54.5% and 63.6% depending on the bacterial strain (Ruchiatan et al., 2023). This situation has driven the exploration of natural-based therapeutic alternatives with both antibacterial and antioxidant activities.

Utilization of natural materials as alternative therapies is increasingly being developed due to their diverse biological activities and relatively lower side effects. One potential Indonesian herbal plant for development is kayu rapet (*Parameria laevigata*) from the Apocynaceae family. This plant has been traditionally used as an anti-ulcer, anti-diarrheal, and wound-healing agent. *P. laevigata* leaves are also used as antiseptics and anti-inflammatories (Saludarez, 2019). Phytochemical analysis showed that *P. laevigata* contains flavonoids, tannins, alkaloids, and saponins, which act as antioxidants and antimicrobials (Muharrami et al., 2020). The ethanol extract of *P. laevigata* was reported to possess antibiofilm activity against *Staphylococcus aureus*, the ability to inhibit *Escherichia coli* biofilm formation, and antifungal activity against *Candida albicans* (Anggraini et al., 2024). These activities demonstrate the potential of *P. laevigata* as an active ingredient in anti-acne preparations.

The success of topical therapy is influenced by the drug delivery system employed (Baskar et al., 2018). The utilization of *P. laevigata* extract in topical preparations faces limitations in active substance penetration due to the presence of the stratum corneum as the primary barrier to active substance delivery. The stratum corneum possesses a "brick-wall" structure consisting of corneocytes and a lipid matrix with a thickness of approximately 10–20 μm, which restricts penetration to small molecules with a molecular weight of less than 500 Da (Lundborg et al., 2018). These characteristics cause most natural compounds to have difficulty penetrating the skin through conventional topical preparations (Baskar et al., 2018).

Dissolving microneedle (DMN) technology offers a minimally invasive approach to overcome stratum corneum penetration barriers, delivering active compounds directly to the target skin layer without causing pain (Arora and Laskar, 2023). With needle dimensions typically below 1000 μm in length and 100–300 μm in base diameter, DMNs have been successfully applied to deliver various plant-derived bioactive compounds transdermally, including shikonin extract (Ning et al., 2021), *Oryza sativa* extract (Chaiwarit et al., 2024), and eugenol (Wang et al., 2024). Clinical evidence further supports their efficacy in acne management: anti-acne DMNs reduced acne volume by 12.34% after 3 days and 22.35% after 7 days without serious adverse effects (Tai et al., 2022), with a favorable safety profile compared to photodynamic therapy (Zhang et al., 2025).

The success of a DMN formulation is greatly influenced by the selection and ratio of the constituent polymers. Various polymers have been widely used in DMN development, such as polyvinyl alcohol (PVA), polyvinylpyrrolidone (PVP), hydroxypropyl methylcellulose (HPMC), carboxymethyl cellulose (CMC), hyaluronic acid, gelatin, and chitosan. Differences in polymer ratios can affect the physical properties of the resulting microneedles, including mechanical strength, needle sharpness, skin penetration ability, dissolution time, and structural stability (Bonfante et al., 2020). Suboptimal ratios can cause needle deformation, structural failure, or uncontrolled dissolution, reducing the effectiveness of active compound delivery (Alrimawi et al., 2024).

To date, no study has reported the integration of *P. laevigata* extract into a DMN-based delivery system for acne therapy. Given its rich bioactive profile and the limitations of conventional topical formulations in delivering plant-derived compounds through the stratum corneum, this study aimed to characterize the phytochemical profile and in vitro antibacterial activity of *P. laevigata* extract against acne-associated pathogens, and to subsequently develop and characterize *P. laevigata*-loaded DMN arrays in terms of their physical and mechanical properties.

2. EXPERIMENTAL SECTION

2.1 Materials

Kayu Rapet (*P. laevigata*, Local Market, Tangerang, Indonesia), polyvinyl alcohol (PVA) (HIMEDIA, China), polyvinylpyrrolidone (PVP) (K30 Povidone, China), Dow Sylgard 184 PDMS (Sylguard, USA), three bacterial strains - *Staphylococcus aureus* (ATCC 12228) and *Cutibacterium acnes* (ATCC 6919) - all obtained from Micropad, Labmart, Indonesia; quercetin (Sigma Aldrich, Germany), 1,1-Diphenyl-2-Picrylhydrazyl (DPPH) (TCI, Japan), vitamin C (CSPC Weisheng Pharmaceutical, China), Ethanol 95% (Onemed, Indonesia), methanol p.a. (CH_3OH, Merck, Germany), distilled water (Aqua DM, Brataco, Indonesia), sodium hydroxide (NaOH) (Cv.Putra Prima, Indonesia), Liberman-Burchad (Merck, Germany), Fe $Cl_3 \cdot 6H_2O$ (Merck, Germany), HCl (Merck, Germany), $AlCl_3$ (Merck, Germany), Mueller Hinton Agar (MHA) (HIMEDIA, China), trichloroacetic acid (TCA) (Merck, Germany).

2.2 Instruments

Stereo microscope (Nikon SMZ 745, Japan), centrifuge (Ohaus FC5706, USA), oven (Memmert UN55, Germany), ultrasonic bath (Ovan, USA), rotary evaporator (IKA RV 10 Digital, Germany), UV-Vis spectrophotometer (Shimadzu Europe UV 1240, Japan), scanning electron microscope (SEM), universal testing machine (UTM) (Zwick Roell, Germany), Fourier transform infrared spectroscopy (FTIR) (FT/IR-4700, Jasco, Tokyo, Japan), autoclave (GEA 50 Lt, Indonesia).

2.3 Extraction of *P. laevigata*

A total of 50 g of *P. laevigata* powder was extracted with 95% ethanol at a solvent-to-material ratio of 1:10 (w/v). Extraction was performed by sonication in an ultrasonic bath at 40°C for 45 min. The filtrate was collected by filtration and concentrated

using a rotary evaporator at 50°C under reduced pressure. The resulting thick extract was then dried in an oven at 50°C for 24 h to obtain a dry extract, and the extraction yield was calculated gravimetrically (More and Arya, 2021).

2.4 Phytochemical Screening

Qualitative phytochemical screening of *P. laevigata* extract was conducted for alkaloids, flavonoids, steroids/triterpenoids, tannins, and saponins using standard colorimetric methods. Alkaloids were detected using Dragendorff's reagent, indicated by an orange to reddish-brown precipitate. Flavonoids were identified by a yellow color change upon addition of NaOH (50%) that faded after acidification. Steroids and triterpenoids were detected using Liebermann–Burchard reagent, indicated by bluish-green and red/purple/brown coloration, respectively. Tannins were identified by a dark blue or blackish-green color upon addition of $FeCl_3$ (10%). Saponins were confirmed by stable foam formation for ≥30 s after vigorous shaking and addition of HCl (2N) (Wiadnyani et al., 2024). All tests were performed on 5 mg of extract in triplicate (n = 3); consistent positive or negative results were obtained across all replicates, confirming reproducibility. Since these screening tests produce binary (positive/negative) outcomes based on colour change criteria, mean ± SD quantification is not applicable; reproducibility is confirmed by concordance across independent replicates.

2.5 Total Flavonoids

Total flavonoid content was determined by the $AlCl_3$ complexation method using quercetin as the reference standard (Chang et al., 2002). A quercetin stock solution (100 ppm) was serially diluted to 2, 4, 8, 10, and 12 ppm. Each standard solution (1 mL) was reacted with methanol p.a., $AlCl_3$ (10%), sodium acetate (1 M), and distilled water, then incubated for 30 min at room temperature. Sample solutions (1% w/v) were treated identically, with a blank prepared by substituting $AlCl_3$ with distilled water. Absorbance was measured at 415 nm, and total flavonoid content was calculated from the quercetin calibration curve and expressed as mg quercetin equivalent per gram of extract (mg QE/g).

2.6 Antioxidant Activity

Antioxidant activity was evaluated using three complementary methods with vitamin C as a positive control. For the DPPH assay, a stock solution of the extract (1000 ppm) was diluted to 10, 15, 20, 35, and 40 ppm, mixed with DPPH solution (1 mL), and incubated for 30 min at room temperature in the dark; absorbance was measured at 517 nm. For the ABTS assay, a radical solution was prepared from 7 mM ABTS and 140 mM $K_2S_2O_8$ incubated for 12–16 h, then diluted to an absorbance of 0.700 ± 0.020 at 728 nm; extract samples (20, 40, 50, and 60 ppm) were mixed with the ABTS solution, incubated for 6 min at 30 °C, and absorbance was measured at 728 nm. For the FRAP assay, extract solution (2400 ppm) was mixed with $FeCl_3$, acetate buffer (pH 6.6), and distilled water, incubated for 30 min in the dark, precipitated with TCA, and centrifuged; absorbance of the supernatant was measured at 593 nm. All IC_{50} values were determined by linear regression analysis.

2.7 Antibacterial Activity

Antibacterial activity of *P. laevigata* extract was evaluated using the well diffusion method against *Staphylococcus aureus* and *Cutibacterium acnes* (Balouiri et al., 2016). Mueller–Hinton agar (MHA) medium (20 mL) was poured into sterile petri dishes and allowed to solidify at room temperature. Bacterial suspensions were prepared in sterile physiological NaCl (0.9% w/v) and adjusted to a turbidity equivalent to the 0.5 McFarland standard. A volume of 100 μL of each suspension was spread evenly across the agar surface using a sterile swab. Wells of 6 mm diameter were aseptically punched into the inoculated agar using a sterile cork borer. Extract solutions were prepared at concentrations of 50, 100, and 150 ppm (w/v) in ethanol, and 50 μL of each solution was dispensed into the corresponding well. Chloramphenicol solution served as the positive control; sterile distilled water served as the negative control. Plates inoculated with *S. aureus* were incubated aerobically at 37 °C for 24 h, while plates inoculated with *C. acnes* were incubated under anaerobic conditions at 37 °C for 48 h. Antibacterial activity was determined by measuring the diameter of the inhibition zone (mm) around each well (Atina et al., 2025). All assays were performed in triplicate (n = 3).

2.8 Microneedle Mold Fabrication

The microneedle male mold was designed using Fusion 360 software in a 7 × 7 array (49 needles) with a height of 1000 μm and inter-needle distance of 300 μm. The design was converted to STL format, processed with slicing software, and printed using a Elegoo Saturn 4 Ultra 3D printer (Elegoo, China). After printing, the male mold was cleaned with resin cleaning solution for 20 min and heated for 1 h to harden and stabilize the structure. The female mold was subsequently fabricated by casting PDMS onto the male master mold at a base-to-curing agent ratio of 10:1, degassed under vacuum for 30 min, and cured at 60 °C for 2 h. After curing, the PDMS female mold was carefully peeled from the male mold and inspected to confirm complete replication of the needle cavity geometry before use in microneedle casting (Economidou et al., 2021).

2.9 Fabrication of Dissolving Microneedles

Microneedles were made by mixing PVA and PVP until the total polymer concentration reached 30% (Lee et al., 2017), and 5% extract was added. The preparation was carried out in eight formulas with varying ratios of PVA and PVP, namely F1–F8 (Table 1). The mixture of each formula was poured into a female mold and then centrifuged for 20 min at 5,000 rpm to ensure the solution was completely filled into the needle cavity. After that, it was dried in a 40 °C oven for 24 h until formed (Cordeiro et al., 2020). The resulting microneedles

Table 1. Composition of Dissolving Microneedle Formulations F1–F8 (Needle Matrix with Total PVA:PVP Content Fixed at 30% w/w) and Backing Layer

Component	F1	F2	F3	F4	F5	F6	F7	F8
Needle matrix (% w/w)								
Parameria laevigata extract	5	5	5	5	5	5	5	5
PVA:PVP ratio[a]	3:5	7:9	1:1	9:7	5:3	2:1	3:1	4:1
Distilled water	65	65	65	65	65	65	65	65
Backing layer (% w/w)								
PVA 10%	10	10	10	10	10	10	10	10
Glycerin	1	1	1	1	1	1	1	1
Distilled water	89	89	89	89	89	89	89	89

[a] Total PVA + PVP content in the needle matrix is fixed at 30% w/w across all formulations; values represent the mass ratio of PVA to PVP within this 30% fraction. All other components are expressed as percentage (w/w) of the total formulation.

were carefully removed with tweezers and stored in a dry.

2.10 Microneedle Characterization

2.10.1 Morphological Characterization

Microneedles were observed using a stereo microscope (Nikon SMZ 745, Japan). Microneedles were placed on a glass slide to determine the height, width, angle, and distance between the needles formed. As a size reference, a 1000 μm micrometer scale was used and observed at the same position to ensure the accuracy of the measurement of the dimensions of the needle structure (Fitaihi et al., 2024; Seetharam et al., 2024).

2.10.2 In Vitro Skin Insertion Simulation

In vitro insertion capability was evaluated using parafilm M (0.16 mm thickness) as a skin simulant. Parafilm sheets were cut to match the microneedle array dimensions and stacked into five layers. The microneedle patch was then pressed uniformly by hand against the parafilm stack, after which each layer was separated and examined under a stereo microscope to count the number of perforations formed. The number of layers successfully perforated was used as an indicator of the insertion capability and mechanical sharpness of the microneedle structure (Justyna et al., 2025; Makvandi et al., 2021).

2.10.3 Scanning Electron Microscopy (SEM)

The microneedle arrays were mounted on circular discs and morphologically characterized using SEM (FEI Quanta™ ESE M, Quanta 200 FEG) at a pressure of 10^{-5} Torr and a voltage of 13 kV. Prior to observation, the samples were coated using an ion beam coating system (PECS™, Gatan) with controlled thickness. Images were observed using XT Microscope Control software with parameter settings such as magnification, tilt angle, spot size, and working distance (Demir et al., 2013).

2.10.4 Mechanical Strength Testing

Microneedle compressive strength or mechanical testing was performed by axial compression on a Universal Testing Machine (Zwick Roell, Germany) using a flat probe covering the entire array. The sample was mounted, the device calibrated, and the zero point was determined when the probe touched the needle apex at a trigger force of 0.02–0.05 N. The probe was then compressed at a rate of 0.5 mm/s to 0.3–0.7 mm of needle height. Fracture force was taken from the peak of the force–displacement curve and reported per array and per needle, along with analysis of stiffness, permanent deformation, and absorbed energy (Rabiei et al., 2021).

2.10.5 Fourier Transform Infrared Spectroscopy (FTIR)

The interactions between the microneedles were investigated using a Fourier transform infrared (FTIR) spectrometer (FT/IR-4700, Jasco, Tokyo, Japan). The microneedles and the material were scanned in transmittance mode from 400 to 4000 cm^{-1} at a resolution of 4 cm^{-1} (Wang et al., 2021).

2.11 In Vitro Release Profile

The in vitro release of *P. laevigata* extract from DMN patches was evaluated using phosphate-buffered saline (PBS, pH 7.4) as the release medium. Prior to analysis, the UV-Vis absorption spectrum of *P. laevigata* extract dissolved in PBS was scanned across the range of 200–800 nm, and a maximum absorption wavelength of 437 nm was identified and selected for quantification. A calibration curve was constructed by dissolving DMN patches of known extract loading concentrations in 5 mL PBS (pH 7.4) and measuring absorbance at 437 nm; absorbance values were plotted against nominal extract concentrations to generate the calibration relationship (R^2 = 0.9423). Each DMN patch was individually placed in 5 mL of PBS at 37 ± 1 °C under gentle stirring. Aliquots of 1 mL were withdrawn at predetermined time intervals (5, 10, 15, 30, 60, 120, 240, 480, 960, and 1440 min) and replaced with an equal volume of fresh PBS to maintain sink conditions. The absorbance of each aliquot was measured at 437 nm using a UV-Vis spectrophotometer, and extract concentration was calculated from the calibration curve. Cumulative release was expressed as a percentage of the total extract content loaded in each patch,

as determined from the calibration. All measurements were performed in triplicate (n = 3).

2.12 Statistical Analysis

All experiments were performed in triplicate (n = 3) unless otherwise stated; Parafilm penetration testing was conducted across three to five replicates per formulation. Data are expressed as mean ± standard deviation (SD). Statistical analysis was performed using IBM SPSS Statistics version 19.0 (IBM Corp., Armonk, NY, USA). Differences in Parafilm penetration performance among DMN formulations at each layer were assessed by one-way analysis of variance (ANOVA) followed by Tukey's honestly significant difference (HSD) post-hoc test. A p-value of < 0.05 was considered statistically significant.

3. RESULTS AND DISCUSSION

3.1 Extraction and Phytochemical Screening

The extraction yield of *P. laevigata* bark was 8.68%, consistent with values reported for ultrasonic-assisted ethanol extraction of polyphenol-rich bark materials under comparable conditions (Bin Mokaizh et al., 2024).

Phytochemical screening revealed the presence of flavonoid s, tannins, saponins, and alkaloids in the *P. laevigata* extract, while steroids were absent (Table 2). Flavonoids and tannins are well-established contributors to antioxidant and anti-inflammatory activity; proanthocyanidins - a tannin subclass previously identified in *P. laevigata* bark-have been reported to support tissue repair through modulation of key signalling pathways (Kamiya et al., 2001; Wu et al., 2025). Alkaloids contribute to antibacterial activity, supporting the potential of this extract as an anti-acne agent (Yan et al., 2021). The absence of steroids is consistent with the preferential extraction of polar and semipolar compounds by ethanol, which is a poor solvent for nonpolar steroids (Arya et al., 2025). The phytochemical profile obtained in this study is in agreement with previously reported findings for *P. laevigata* (Muharrami et al., 2020).

3.2 Total Flavonoids

The total flavonoid content of *P. laevigata* extract was determined spectrophotometrically using the $AlCl_3$ colorimetric method with quercetin as the reference standard. The quercetin calibration curve demonstrated acceptable linearity (R^2 = 0.9–865) across the tested concentration range. The total flavonoid content of the extract was 0.120 ± 0.002 mg QE/g extract (Table 3), with a low standard deviation indicating good inter-replicate precision. This result confirms the presence of quantifiable flavonoids in *P. laevigata* extract, consistent with previous reports on the polyphenolic composition of this plant (Muharrami et al., 2020; Wu et al., 2025). The flavonoid content, while moderate, supports the rationale for incorporating this extract into a DMN delivery system capable of enhancing transdermal penetration of bioactive compounds.

3.3 Antioxidant Activity (DPPH, ABTS, and FRAP)

Antioxidant activity of *P. laevigata* extract was evaluated using three complementary methods (Table 3). The DPPH assay yielded an IC_{50} of 40.98 ppm (R^2 = 0.9869), categorised as strong antioxidant activity, while the ABTS assay produced an IC_{50} of 46.92 ppm (R^2 = 0.988), also within the strong category (Dontha, 2016). For comparison, the positive control vitamin C yielded IC_{50} values of 9.2 ± 2.21 ppm (DPPH) and 11.21 ± 3.06 ppm (ABTS), indicating that *P. laevigata* extract exhibited approximately 4.5-fold (DPPH) and 4.2-fold (ABTS) lower radical-scavenging potency than ascorbic acid on a concentration basis, a ratio consistent with polyphenol-rich bark extracts of comparable phytochemical composition (Utami et al., 2024). The consistency between DPPH and ABTS results confirms that the extract exerts antioxidant activity through both hydrogen atom transfer and single electron transfer mechanisms (Santos-Sánchez et al., 2019). The total antioxidant capacity measured by FRAP was 70.238 mg AAE/g extract, reflecting substantial ferric ion-reducing capacity attributable to the polyphenolic content of the extract, particularly proanthocyanidin A-2 and cinnamtannin B1 previously identified in *P. laevigata* bark (Kamiya et al., 2001). For comparison, *Etlingera elatior* leaf extract reported a FRAP value of 78.52 mg AAE/g (Utami et al., 2024), indicating that *P. laevigata* exhibits competitive antioxidant potential as a natural ingredient. The antioxidant capacity of the extract is directly relevant to its anti-acne rationale: elevated reactive oxygen species (ROS) and oxidative stress are well-established contributors to acne pathogenesis, with clinical evidence demonstrating decreased superoxide dismutase (SOD) activity and increased malondialdehyde (MDA) levels in acne patients compared to healthy controls, confirming impaired antioxidant defence in this condition (Popa et al., 2023; J.R. et al., 2022). Furthermore, antioxidant supplementation has been shown to improve acne outcomes by suppressing lipid peroxidation and inhibiting pro-inflammatory cytokine expression (Mawu et al., 2025). These findings collectively validate the biochemical rationale for incorporating antioxidant-rich *P. laevigata* extract into the DMN system for acne therapy, while full pharmacodynamic validation via cell-based ROS quantification remains an important future direction. Collectively, the convergent results across all three methods support the antioxidant basis for the anti-acne application of this extract within the DMN system.

3.4 Antibacterial Activity of *P. laevigata* Extract

Antibacterial activity of *P. laevigata* extract against *Staphylococcus aureus* and *Cutibacterium acnes* was evaluated by well diffusion at concentrations of 50, 100, and 150 ppm (Figure 1; Table 4). Against *S. aureus*, no inhibition zone was observed at 50 ppm, while total inhibition zone diameters of 8.22 ± 0.03 mm and 8.44 ± 0.08 mm were recorded at 100 and 150 ppm, respectively. Against *C. acnes*, inhibition zones were detected at all tested concentrations: 7.77 ± 0.37 mm at 50 ppm, 8.30 ± 0.14 mm at 100 ppm, and 8.46 ± 0.28 mm at 150 ppm. The positive control (chloramphenicol) produced inhibition zones

Table 2. Phytochemical Screening

Phytochemical Screening	Reagent	Result	Changes
Saponins	HCl 2N	+	Stable foam forms after shaking
Steroids	Liberman–Burchad	–	No green or blue color change occurs
Tanins	$FeCl_3$ (10%)	+	A blackish-green color forms
Alkaloids	Dragendorff	+	A reddish-brown precipitate forms
Flavonoids	NaOH (50%)	+	The solution turns yellow

Table 3. Phytochemical Content and Antioxidant Activity of *P. laevigata* Extract

Parameter	Unit	Value (mean ± SD, n = 3)
Extraction yield	%	8.68
Total flavonoid content (TFC)	mg QE/g extract	0.120 ± 0.002
DPPH scavenging activity (IC_{50})	ppm	40.98 ± 4.32
DPPH scavenging activity (IC_{50}) - vitamin C (positive control)	ppm	9.2 ± 2.21
ABTS scavenging activity (IC_{50})	ppm	46.92 ± 3.25
ABTS scavenging activity (IC_{50}) - vitamin C (positive control)	ppm	11.21 ± 3.06
FRAP reducing capacity	mg AAE/g extract	70.24 ± 6.41

Table 4. Inhibition Zone Diameters of *Parameria laevigata* Bark Extract Against Acne-Associated Bacteria by Disc Diffusion Method

Test Bacteria	Concentration	Mean Inhibition Zone Diameter ± SD (mm, *n* = 3)
Staphylococcus aureus	50 ppm	0 ± 0
	100 ppm	8.22 ± 0.03
	150 ppm	8.44 ± 0.08
	Positive control	10.86 ± 0.03
	Negative control	0 ± 0
Cutibacterium acnes	50 ppm	7.77 ± 0.37
	100 ppm	8.30 ± 0.14
	150 ppm	8.46 ± 0.28
	Positive control	10.57 ± 0.17
	Negative control	0 ± 0

Positive control: chloramphenicol solution; Negative control: sterile distilled water. Values represent total inhibition zone diameter including well diameter (6 mm).

of 10.86 ± 0.03 mm against *S. aureus* and 10.57 ± 0.17 mm against *C. acnes*, while the negative control produced no inhibition. The dose-dependent increase in inhibition zone diameter confirms a concentration–response relationship for both organisms. Based on the classification proposed by Davis and Stout (1971), inhibition zone diameters of 5–10 mm indicate moderate antibacterial activity; accordingly, *P. laevigata* extract demonstrated moderate activity against both organisms at 100 and 150 ppm, and moderate activity against *C. acnes* at 50 ppm, while no activity was recorded against *S. aureus* at the lowest concentration tested. The slightly greater sensitivity of *C. acnes* relative to *S. aureus* may reflect differences in cell envelope composition and susceptibility to polyphenolic compounds. The antibacterial activity is attributed to flavonoids and proanthocyanidins - including proanthocyanidin A-2 and cinnamtannin B1 previously identified in *P. laevigata* bark - which disrupt bacterial membrane integrity and inhibit cell wall permeability (Kamiya et al., 2001; Chaves et al., 2020).

Although the activity observed at the tested concentrations remains moderate relative to the antibiotic positive control, this outcome must be interpreted in the context of the intended delivery route. The well diffusion assay inherently underestimates the antibacterial performance of compounds destined for DMN delivery, since extract loaded into the well must first diffuse through the surrounding agar matrix - a process that is particularly restricted for high-molecular-weight polyphenols such as proanthocyanidins, which exhibit limited diffusivity in hydrophilic gels due to their extensive hydroxyl-mediated interactions with the matrix (Chaves et al., 2020; Kamiya et al., 2001). DMN application bypasses this diffusional barrier by depositing the loaded dose directly into the micro-channels of the viable epidermis, which may enhance local bioavailability of the active compounds at the pilosebaceous unit compared to conventional topical application where permeation is limited by the intact stratum corneum (Hashempur et al., 2025; Zhang et al., 2024). The well diffusion method employed in this study is a widely validated approach for initial antimicrobial screening of liquid plant extract preparations against reference strains (Balouiri et al., 2016), and inhibition zone diameter represents the standard quantitative output for this methodology. Regarding the ethanol solvent effect, the concentration of residual ethanol introduced per well was negligible relative to the agar

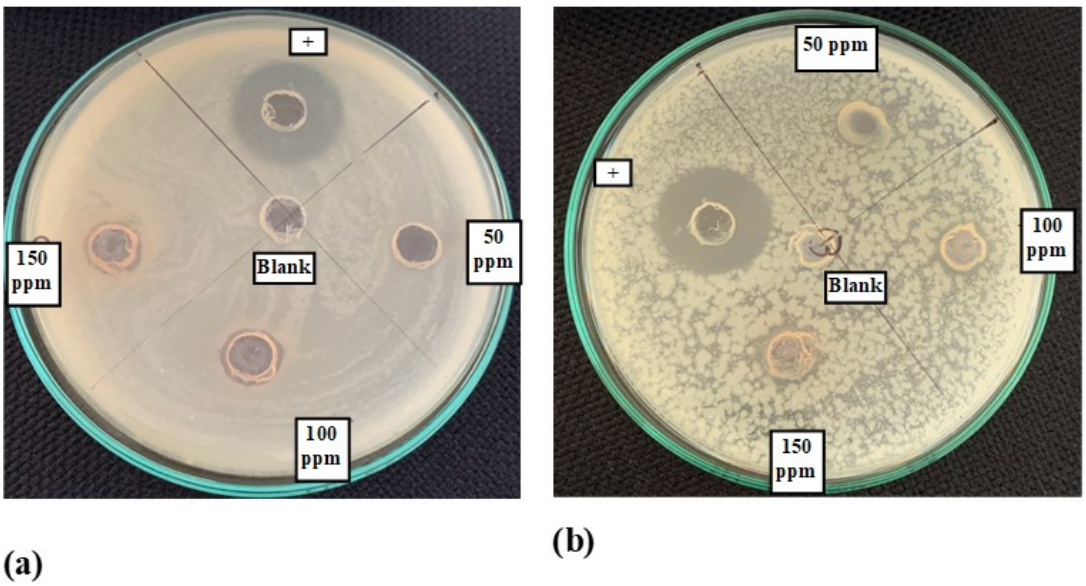

Figure 1. Antibacterial Activity of the Extract Against (a) *Staphylococcus aureus* (b) *Cutibacterium acnes*

volume, resulting in an effective ethanol concentration well below the 2% v/v threshold for intrinsic antimicrobial activity; the negative control confirmed the absence of spontaneous inhibition.

3.5 Microneedle Mold

The fabricated PDMS female mold produced a complete 7×7 array cavity system corresponding to 49 pyramidal needles, replicated from the resin-based 3D-printed male mold (Figure 2a-c). The male mold exhibited a mean needle height of 781.22 ± 3.25 μm and a base width of 390.52 ± 2.19 μm, representing approximately 22% reduction in height and 30% increase in base width relative to the original 3D design specifications of 1000 μm height and 300 μm base width. This dimensional deviation from the digital design is attributable to three main factors: first, the XY resolution of the 3D printer (19×24 μm) introduces a staircase discretisation effect in the pyramidal geometry, truncating sub-resolution tip features and broadening the effective base width; second, resin shrinkage during UV curing typically reduces final dimensions by 10–20% for stereolithographic resins (Jiang and Drummer, 2022); and third, the discretisation of the pyramidal slope at discrete XY voxel steps may also contribute to apparent base widening at the mold–printer interface. Although the Z-axis layer thickness of 25 μm is theoretically capable of reproducing heights up to 1000 μm (requiring 40 layers), the combined XY discretisation and resin shrinkage effects dominate the final male mold dimensions. The resulting PDMS female mold (Figure 2d) additionally undergoes minor thermal shrinkage during curing (typically 1–3%), which further modifies the replicated cavity dimensions relative to the male template (Oliveira et al., 2024); as PDMS cavities were not directly measurable due to their concave geometry, this contribution was inferred from DMN dimensional measurements presented in Section 3.6. Despite these cumulative deviations, the fabricated mold cavity remains within the functional dimensional range established for transdermal DMN applications (height: 300–1000 μm; base width: 100–300 μm) (Luo et al., 2023). The PDMS mold surface was smooth and free of air bubbles, confirming homogeneous mixing of the PDMS base and curing agent and successful negative replication of the male template.

3.6 Croneedle Morphology

Stereomicroscopic evaluation revealed that the PVA:PVP ratio markedly influenced DMN needle morphology across all formulations (Table 5; Figure 3). One-way ANOVA confirmed statistically significant differences in both needle height ($F(8, 18) = 112.55$, $p < 0.001$) and base width ($F(8, 18) = 58.85$, $p < 0.001$) across the master mold and eight DMN formulations, and Tukey HSD post hoc analysis demonstrated that every DMN formulation produced needles significantly shorter and narrower than the master mold ($p < 0.001$). F2 produced the optimal morphology, with all 49 needles fully formed in a uniform 7×7 array (Figure 3a), a mean height of 581.0 ± 1.7 µm, a base width of 322.3 ± 0.6 µm, and no visible physical defects. The exceptionally low standard deviations obtained for F2 reflect well-matched solution viscosity that enabled complete mold cavity filling and uniform needle replication. F2 exhibited the smallest reduction relative to the master template - approximately 25.6% in height and 17.5% in base width - and was statistically superior to F5, F6, F7, and F8 in retaining needle height ($p < 0.05$), and superior to all other formulations except F5, F6, and F8 in retaining base width ($p < 0.05$). This cumulative dimensional loss is attributable to shrinkage occurring at two sequential stages: thermal shrinkage of the PDMS female mold during curing (~1–3%), followed

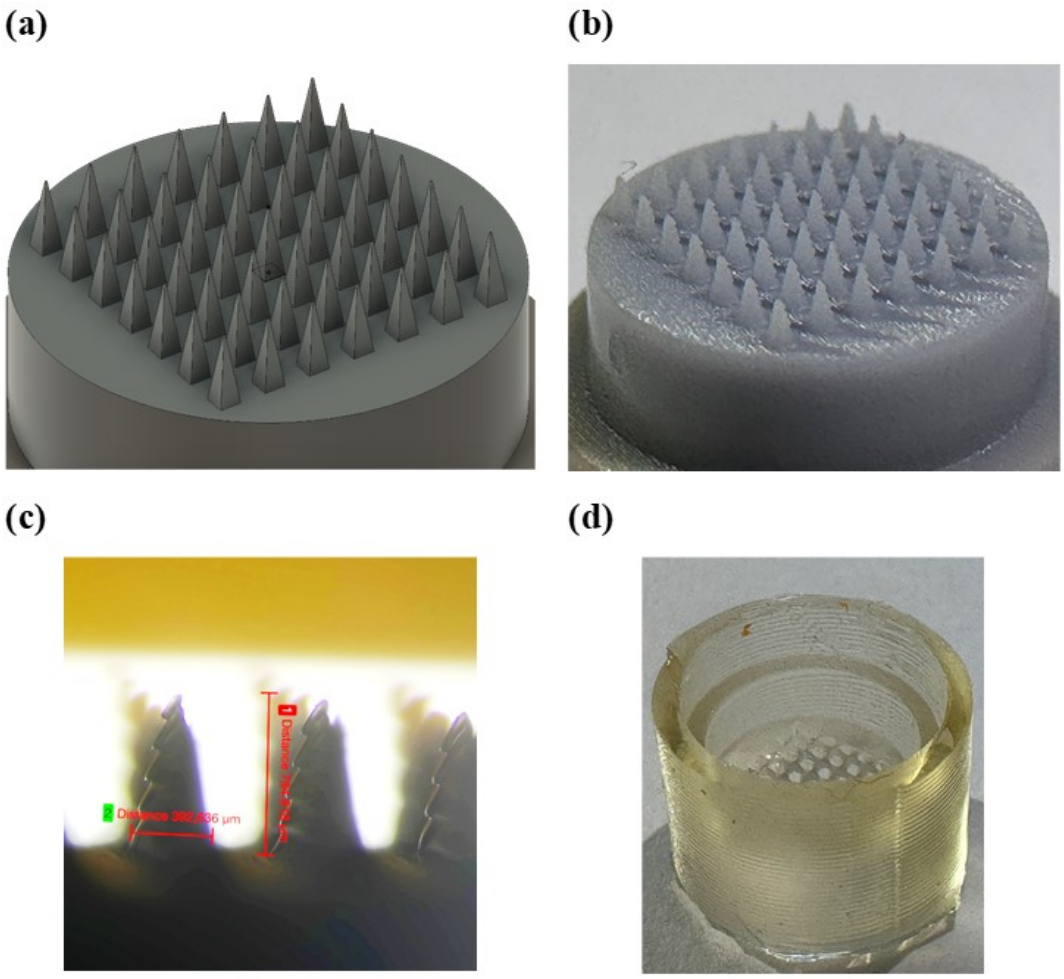

Figure 2. Fabrication Stages of the Microneedle Mold: (a) 3D Design of the Master Mold Generated Using Fusion 360; (b) 3D-Printed Resin Male Mold; (c) Stereomicroscopic Image of the Male Mold Needle Structure Showing Measured Needle Dimensions; (d) Final PDMS Female Mold Replicated from the Male Mold

by aqueous solvent evaporation and polymer matrix consolidation during DMN drying, which induces further volumetric contraction of the PVA/PVP matrix as it solidifies within the mold cavity (Oliveira et al., 2024).

In contrast to F2, suboptimal PVA:PVP ratios produced four distinct types of morphological defects (Figure 3b): air bubbles (observed in F1 and F5), attributed to entrapment during the mold-filling process that disrupts matrix continuity and may compromise mechanical integrity (Tijani et al., 2023); broken needles (F3), consistent with excessive solution viscosity impeding complete flow into the narrow mold tip cavities, resulting in structurally weak needles prone to shear failure during demolding; incomplete tip formation (F4), likewise arising from viscosity-driven incomplete filling of the apical mold regions; and reduced needle count (F6–F8: 39–43 needles), indicating that high polymer concentrations increased solution viscosity beyond the threshold for reliable cavity filling (Amano et al., 2025). Formulations with the highest PVA content (F6, F7, and F8) exhibited the most pronounced height reduction, with F6 and F8 reaching mean heights of 496.8 ± 2.4 µm and 498.7 ± 1.5 µm respectively - significantly shorter than F1–F4 ($p < 0.05$) and representing a 36.2–36.4% loss relative to the master mold. F7 further displayed the narrowest base width (234.3 ± 5.1 µm), a 40.0% reduction from the master template and significantly different from all other formulations ($p < 0.001$), consistent with severe capillary retention of the highly viscous solution at the mold cavity entrance. Across all formulations, DMN needle heights ranged from 496.8 to 581.0 µm and base widths from 234.3 to 322.3 µm, all within the accepted range for stratum corneum penetration without reaching the dermis (Arora and Laskar, 2023).

Table 5. Physical Morphology and Dimensions of *P. laevigata*-Loaded DMN Arrays Across Formulations (n = 3)

Formula	Needles Formed	Needle Height (μm)[a]	Base Width (μm)[a]	Physical Defects
Master Mold	49	781.22 ± 3.25	390.52 ± 2.19	None
F1	49	568.3 ± 3.2^{b}	288.7 ± 11.0^{c}	Air bubbles
F2	49	581.0 ± 1.7^{b}	322.3 ± 0.6^{b}	None
F3	49	566.7 ± 7.6^{b}	290.7 ± 8.6^{c}	Broken needles
F4	49	545.0 ± 10.0^{b}	290.3 ± 8.1^{c}	Incomplete tip formation
F5	49	507.7 ± 19.4^{d}	304.3 ± 14.0^{bc}	Air bubbles
F6	43^{e}	496.8 ± 2.4^{d}	302.8 ± 16.2^{bc}	Incomplete needle count
F7	39^{e}	518.7 ± 35.9^{d}	234.3 ± 5.1^{a}	Incomplete needle count
F8	41^{e}	498.7 ± 1.5^{d}	298.0 ± 3.5^{bc}	Incomplete needle count

[a] Values are expressed as mean ± standard deviation (n = 3). Different superscript letters within the same column indicate statistically significant differences between groups (one-way ANOVA followed by Tukey HSD *post hoc* test, $p < 0.05$).

[e] Incomplete array - fewer than the expected 49 needles formed per patch.

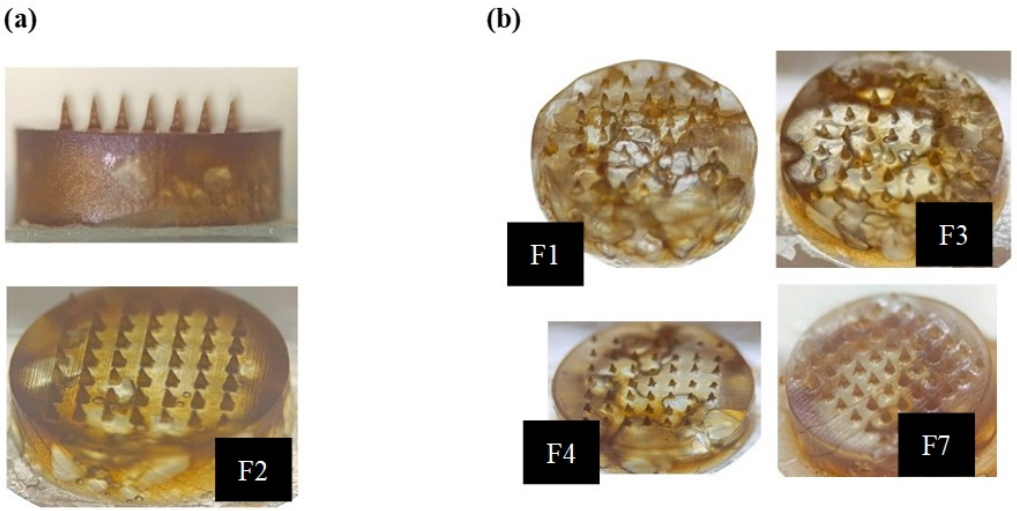

Figure 3. Stereomicroscopic Characterization of *P. laevigata*-Loaded DMN Morphology. (A) Side View (Top) and Top View (Bottom) of the Optimum Formulation F2. (B) Representative Morphological Defects Observed in Suboptimal Formulations: Air Bubbles (F1), Broken Needles (F3), Incomplete Tip Formation (F4), and Incomplete Needle Count (F7)

3.7 Microneedle Penetration

Parafilm penetration testing demonstrated statistically significant differences in mechanical performance across formulations at both layer 2 and layer 3 (one-way ANOVA: $F = 5.02$, $p = 0.0016$ and $F = 3.32$, $p = 0.0145$, respectively; Table 6; Figure 4). F2 achieved the highest penetration consistency, with 97.45 ± 1.02% penetration at layer 2 - the lowest SD among all formulations - and 60.20 ± 33.84% at layer 3, maintaining detectable penetration to layer 4 (13.27 ± 13.89%). Post-hoc Tukey HSD analysis revealed that F2 differed significantly from F4 and F5 at layer 2 ($p = 0.0097$ and $p = 0.0103$, respectively) and from F5 and F7 at layer 3 ($p = 0.0147$ and $p = 0.0220$, respectively), while no significant differences were observed between F2 and F1, F3, F6, or F8. Although F1, F3, and F6 reached layer 4, their penetration depth was accompanied by higher inter-replicate variability (SD: 6.12–18.48% at layer 2) compared to F2 (SD: 1.02%), indicating less reproducible mechanical performance. F7 penetrated only to layer 2 (79.77 ± 16.40%), and F4 and F5 showed markedly reduced second-layer penetration (48.02 ± 36.14% and 48.33 ± 16.14%, respectively), consistent with insufficient needle rigidity in PVP-dominant formulations. The superior penetration of F2 reflects the balanced mechanical contribution of PVA and PVP: PVA confers structural rigidity sufficient for stratum corneum penetration, while PVP provides flexibility that prevents brittle fracture under compressive load. Penetration to four Parafilm layers exceeds the two-to-three layer threshold considered adequate for stratum corneum penetration (Mohammadi et al.,

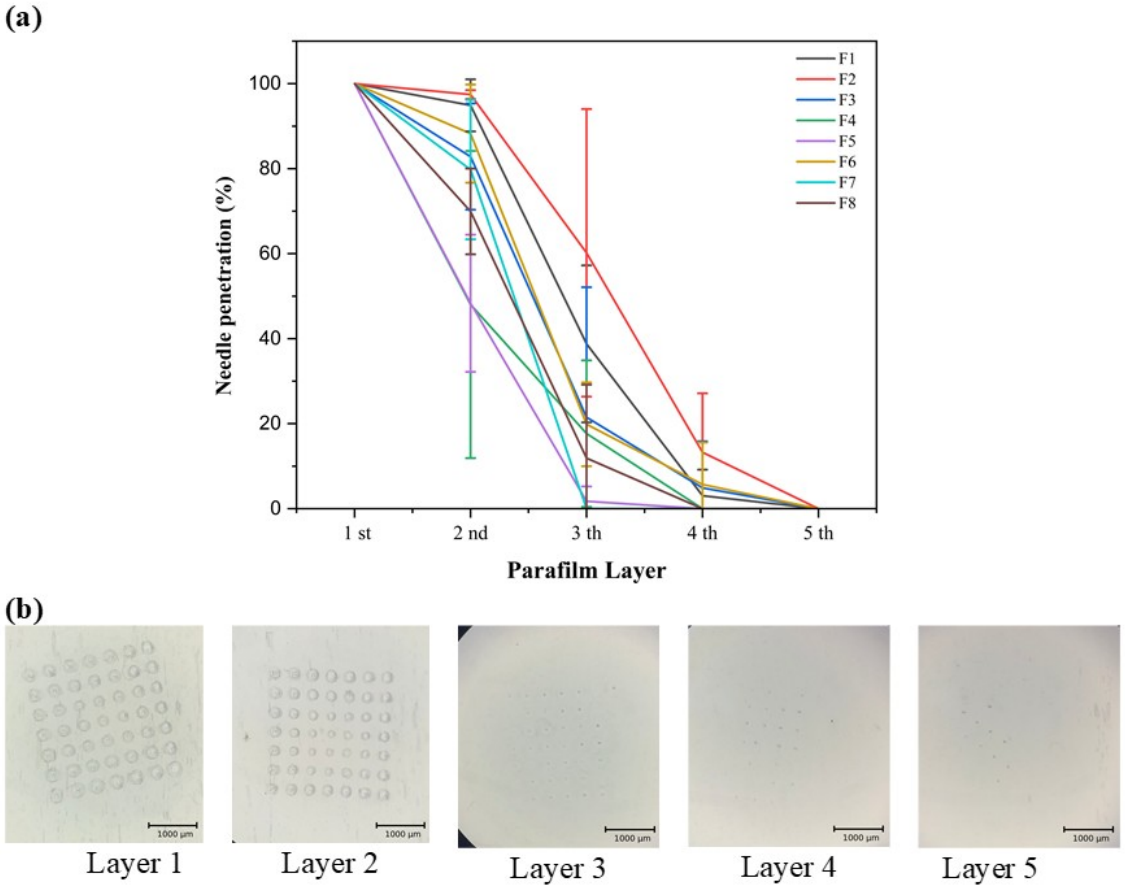

Figure 4. Parafilm Insertion Test of the Microneedle: (A) Percentage of Needle Penetration for Each Formula (F1–F8) and (B) Representative Images of Penetration Holes From F2 Across Layers 1 To 5. Data are Presented as Mean ± SD (n=3)

Table 6. Parafilm Penetration Performance of DMN Arrays Across Formulations (% Needles Penetrating Each Layer, Man ± SD)

Formula	Layer 1	Layer 2	Layer 3	Layer 4	Max. Layer
F1	100 ± 0	94.90 ± 6.12^a	38.78 ± 18.48^a	3.06 ± 6.12^a	4
F2	100 ± 0	97.45 ± 1.02^a	60.20 ± 33.84^a	13.27 ± 13.89^a	4
F3	100 ± 0	82.84 ± 12.48^a	21.50 ± 30.61^a	4.90 ± 10.95^a	4
F4	100 ± 0	48.02 ± 36.14^b	17.67 ± 17.23^a	0	3
F5	100 ± 0	48.33 ± 16.14^b	1.74 ± 3.49^c	0	3
F6	100 ± 0	88.24 ± 11.54^a	19.85 ± 9.86^a	5.69 ± 9.86^a	4
F7	100 ± 0	79.77 ± 16.40^a	0	0	2
F8	100 ± 0	69.94 ± 10.08^a	11.90 ± 2.55^b	0	3

Note: Penetration percentage was calculated as the ratio of perforations formed on each Parafilm layer to the total number of needles formed in each DMN array (refer to Table 5 for actual needle counts per formulation: F1–F5 = 49 needles; F6 = 43; F7 = 39; F8 = 41), expressed as a percentage. Values represent mean ± SD across independent replicates. Within each column, values sharing the same superscript letter are not significantly different, whereas values with different superscript letters indicate statistically significant differences ($p < 0.05$) as determined by one-way ANOVA followed by Tukey's honestly significant difference (HSD) post-hoc test. Max. Layer = the deepest Parafilm layer reached by at least one needle in the array.

2021) and is consistent with or superior to reported PVA/PVP DMN systems with comparable needle dimensions (Lundborg et al., 2018). Based on the combination of superior morphological completeness, dimensional uniformity, and reproducible penetration performance, F2 was selected as the optimal formulation and is hereafter referred to as DMN.

3.8 Scanning Electron Microscopy

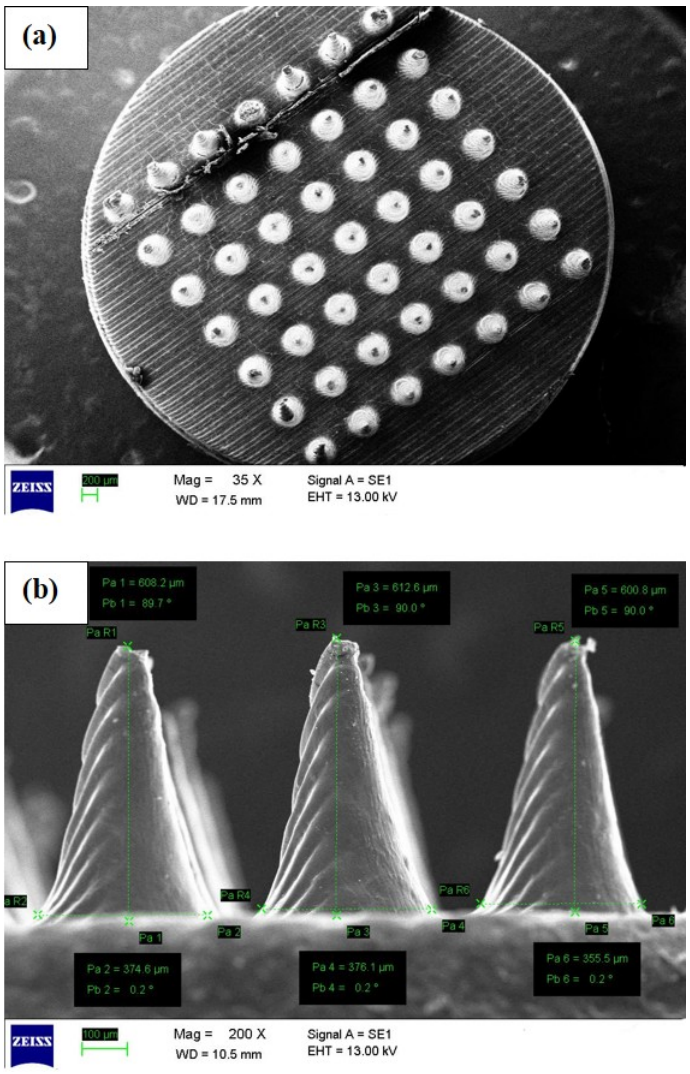

Figure 5. SEM Micrographs of Microneedle Formula 2 (F2): (A) Top View Morphology and (B) Side View Showing Needle Dimensions

SEM analysis of DMN arrays confirmed the sharp, pyramidal needle morphology observed by stereomicroscopy, with greater dimensional resolution (Figure 5a-b). Needle heights measured 608–613 µm and base widths 355–376 µm by SEM, showing good agreement with stereomicroscopic measurements (581.0 ± 1.7 µm height; 322.3 ± 0.6 µm width). The marginal dimensional differences (~5%) between techniques are attributable to sample-to-sample variation and differences in measurement reference points, and fall well within acceptable ranges for microneedle characterisation. The 49-needle array was complete and regularly arranged, with symmetrical tip geometry and a relatively smooth needle surface. The smooth surface indicates homogeneous dispersion of extract within the PVA/PVP matrix during fabrication, with minimal phase separation or surface aggregation. The sharp pyramidal tip geometry is consistent with the penetration performance demonstrated in Parafilm testing and supports effective stratum corneum penetration upon application (Makvandi et al., 2021).

3.9 Mechanical Properties

Compression testing of DMN arrays demonstrated a characteristic biphasic force–displacement response with a critical failure point at 65 mN per needle occurring at 670 µm displacement (Figure 6, red marker). Three distinct mechanical stages were observed during compression. In the initial stage (0–200 µm displacement), force response remained minimal (< 5 mN per needle), reflecting the progressive flattening of the sharp pyramidal tips, which present very small apical contact area and therefore negligible resistance to low compressive loads. From 200 to 670 µm, force increased progressively and non-linearly, corresponding to the elastic–plastic deformation phase of the needle shaft, during which the applied load was distributed across the bulk pyramidal structure until the critical buckling threshold was reached. Beyond 670 µm, a brief force plateau at approximately 65–70 mN per needle was observed, indicative of needle yielding, followed by a steep force increase beyond 0.8 mm as the compression head engaged the patch base, marking the onset of matrix densification rather than continued needle-specific deformation.

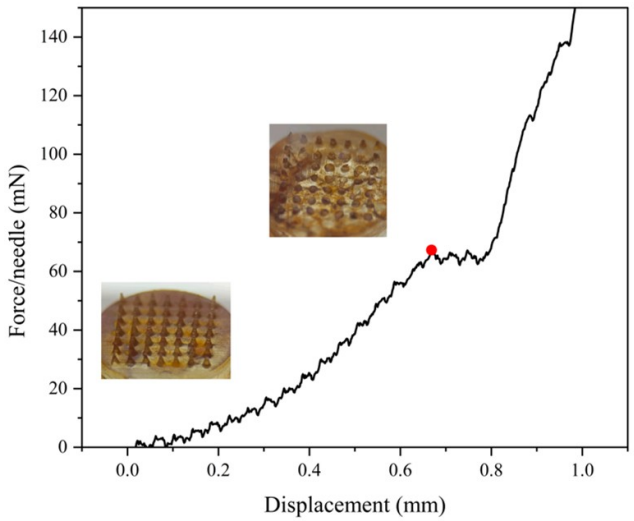

Figure 6. Mechanical Strength Profile of DMN (F2) Under Compression Test

Stereomicroscopic inspection before and after compression, shown as insets in Figure 6, confirmed the predicted failure mode. Prior to compression, the DMN exhibited well-defined,

Table 7. Kinetics of DMN Release

Model	R^2	K	n	Interpretation
Zero-order	0.5566	–	–	Poor fit
First-order	0.2175	–	–	Poor fit
Higuchi	0.6106	0.8579%·min$^{-1/2}$	0.5 (fixed)	Moderate fit
Korsmeyer–Peppas	0.7199	8.79 %·min^{-2}	0.488	Predominantly Fickian diffusion with minor polymer relaxation

sharp pyramidal tips arranged uniformly across the 7 × 7 array (left inset), consistent with the SEM observations reported above. Following compression to the failure point, the needle tips were visibly blunted and flattened (right inset), with the overall array geometry preserved and no evidence of catastrophic fracture, needle detachment, or base-level structural collapse. This localised tip deformation without full structural failure is characteristic of buckling-mode failure, in which compressive stress exceeds the critical load for elastic stability and initiates plastic deformation concentrated at the needle apex (Tsuboko et al., 2024).

The recorded critical failure force of 65 mN per needle falls within the 30–100 mN per needle range required for effective stratum corneum penetration (Tsuboko et al., 2024), confirming that DMN possesses adequate mechanical integrity for transdermal application without premature structural collapse during insertion (Alrimawi et al., 2024; Amano et al., 2025). Importantly, the retention of the 7 × 7 array geometry post-compression, combined with the localisation of deformation exclusively to the tip region, indicates that the balanced PVA/PVP matrix in DMN provides sufficient bulk rigidity to preserve patch integrity throughout the application process, while allowing controlled tip-level deformation conducive to skin dissolution-mediated drug release.

3.10 FTIR Spectroscopy

The FTIR spectra of the individual components and the optimized DMN formulation (F2) are presented in Figure 7. The PVA spectrum exhibited characteristic bands at 3273 cm^{-1} (O–H stretching), 2925 cm^{-1} (C–H stretching), 1606 cm^{-1} (O–H bending), 1519–1366 cm^{-1} (C–H deformations), 1280 cm^{-1} (C–O stretching), and 820 and 765 cm^{-1} (skeletal vibrations), consistent with reported PVA profiles (Teodorescu et al., 2019; Oh et al., 2022). The PVP spectrum displayed bands at 3389 cm^{-1} (N–H/O–H), 2953 cm^{-1} (C–H stretching), 1494 cm^{-1} (C=O amide I of the lactam ring), 1461–1288 cm^{-1} (C–H and C–N deformations of the pyrrolidone ring), and 1041 and 1018 cm^{-1} (C–N ring vibrations), in agreement with the vinylpyrrolidone backbone (Aisyah et al., 2024; Kurakula and Rao, 2020). The *P. laevigata* extract showed a broad O–H band at 3294 cm^{-1} attributable to phenolic hydroxyls of epicatechin-based condensed tannins (parameritannin A-1 and A-2) as the dominant bark constituents (Kamiya et al., 2001),

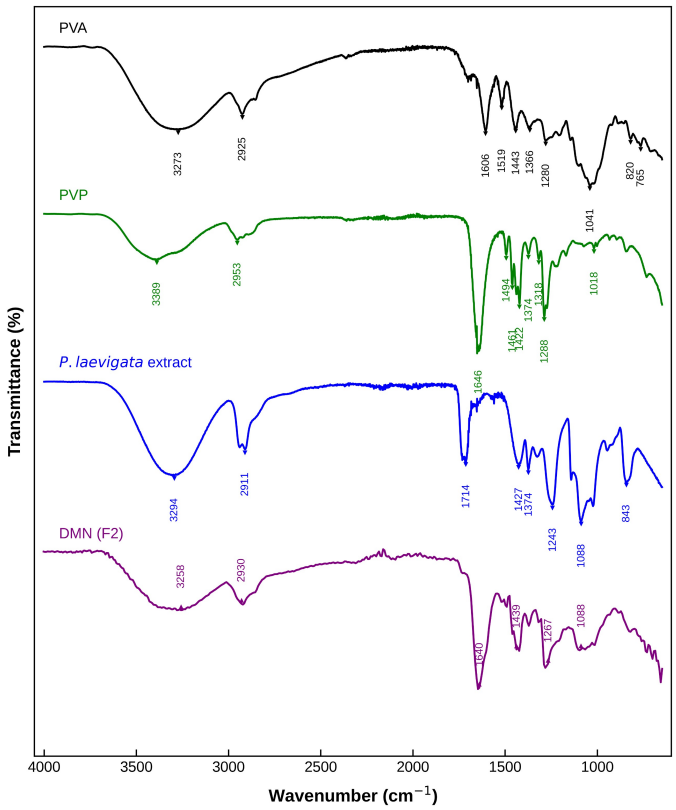

Figure 7. FTIR Spectra of PVP, PVA, *P. laevigata* Extract, and DMN

with additional bands at 1646 cm^{-1} (aromatic C=C of the catechin B-ring; Ciobanu et al., 2023), 1714 cm^{-1} (carbonyl of hydrolyzable tannin moieties), 1243 cm^{-1} (C–O–C interflavanic ether of type-A proanthocyanidins), and 1088 cm^{-1} (C–O polyphenolic stretching) (Kamiya et al., 2001; Luo et al., 2019).

The DMN (F2) spectrum retained all characteristic bands of its components, with the O–H stretching band shifting bathochromically to 3258 cm^{-1} - a displacement of 36 cm^{-1} from the extract and 15 cm^{-1} from PVA - indicative of intermolecular hydrogen bonding between phenolic hydroxyls of *P. laevigata* proanthocyanidins and the carbonyl of PVP's lactam ring and hydroxyl groups of PVA (Teodorescu et al., 2019).

No new absorption bands were detected and no existing bands were eliminated, confirming the absence of new covalent bond formation and establishing the physicochemical compatibility and biocompatibility of the extract–polymer system (Aisyah et al., 2024; Oh et al., 2022).

3.11 In Vitro Release Profile

The cumulative release profile of *P. laevigata* extract from DMN patches in PBS (pH 7.4, 37 ± 1°C) over 1440 min is presented in Figure 8. The release pattern demonstrated a biphasic behaviour, characterised by an initial rapid burst phase followed by a sustained plateau phase. Within the first 10 min, approximately 10.81% of the loaded extract was released, increasing substantially to 43.68% by 120 min, representing the burst release phase. This initial burst release is mechanistically explained by the structural geometry of the DMN patch, as evidenced by SEM observations (Figure 5a-b). The sharp, pyramidal needle tips - with heights of 608–613 μm and base widths of 355–376 μm - present a high surface area-to-volume ratio upon contact with the release medium, facilitating rapid and simultaneous dissolution across all 49 needle tips and creating multiple parallel diffusion fronts that collectively drive the burst release observed within the first 120 min (Yang et al., 2021). Furthermore, during the fabrication process, solvent evaporation dynamics within the mould cavity promote preferential accumulation of extract molecules near the needle tip surfaces, establishing a steep initial concentration gradient that further accelerates early-phase diffusion into the PBS medium. In contrast, the backing layer of the DMN patch requires a substantially longer period for complete hydration, progressive swelling, and polymer chain relaxation before the deeply entrapped extract molecules can diffuse outward through the expanding PVA/PVP network, accounting for the transition to the sustained release phase observed beyond 120 min (Onesto et al., 2020).

Beyond 120 min, the cumulative release plateaued, reaching 56.48% at 1440 min. The absence of complete release over 24 h suggests that a fraction of the extract remained entrapped within incompletely dissolved polymer regions or formed insoluble aggregates within the PBS medium, a phenomenon previously reported for polyphenol-rich plant extracts under aqueous sink conditions (Briuglia et al., 2014). Values recorded at 480 and 960 min showed negligible variation relative to adjacent time points, consistent with the plateau phase rather than progressive release. The sustained release profile over 24 h is consistent with the kinetic requirements for prolonged topical anti-acne therapy; however, whether this in vitro release pattern translates to sustained compound availability within the viable skin layers remains to be confirmed through ex vivo permeation studies.

To elucidate the underlying release mechanism, cumulative release data were fitted to four mathematical kinetic models: zero-order, first-order, Higuchi, and Korsmeyer–Peppas (Table 7). The Korsmeyer–Peppas model yielded the highest coefficient of determination (R^2 = 0.7199), with a release rate constant K = 8.79 %·min^{-n} and diffusion exponent n = 0.4880, followed by the Higuchi model (R^2 = 0.6106; K =), while zero-order (R^2 = 0.5566) and first-order (R^2 = 0.2175) models showed substantially weaker fits. The Korsmeyer–Peppas model was therefore selected as the most representative descriptor of the release kinetics. The very low R^2 of the first-order model confirms that the release rate is not governed by the concentration gradient of the remaining extract within the matrix, but is instead primarily determined by the physical dissolution behaviour of the polymer (Yazdani et al., 2022). The moderate fit of the Higuchi model suggests that diffusion through the dissolving matrix contributes partially to the overall release mechanism (Hashempur et al., 2025). The diffusion exponent n = 0.4880 falls marginally above the Fickian diffusion threshold for flat membrane geometry (n = 0.45), placing the release mechanism at the boundary between Fickian and anomalous transport, wherein molecular diffusion is the predominant mechanism accompanied by a minor contribution of polymer chain relaxation through swelling of the hydrophilic PVA/PVP matrix (Ali et al., 2020).

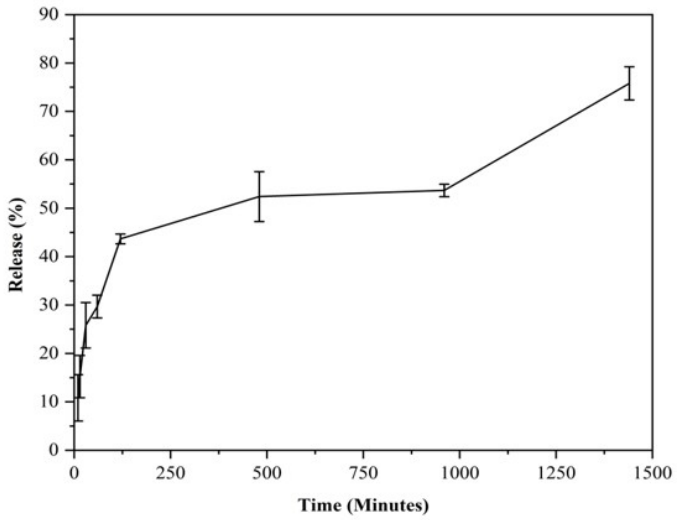

Figure 8. Cumulative Release Profile of the Extract from DMN (F2) Over Time. Data are Presented as Mean ± SD (n=3)

The biphasic release behaviour, combined with Korsmeyer–Peppas kinetics, supports the suitability of this DMN system for controlled transdermal delivery in acne therapy, providing an initial therapeutic dose through burst release from the needle tips, followed by sustained delivery from the dissolving backing layer over 24 h. In this study, UV-Vis spectrophotometry at 437 nm was utilized as a robust and widely accepted initial screening method to evaluate the macroscopic release profile of total flavonoid compounds from the complex PVA/PVP matrix. The calibration approach, which employed DMN patches of known loading concentrations to account for matrix effects, yielded an acceptable linearity (R^2 = 0.9423) for semi-quantitative estimation. This macroscopic evaluation successfully captured the overall release kinetics and confirmed the

sustained delivery capability of the DMN system, despite potential minor background absorption from the dissolving polymer excipients (Shimamoto et al., 2019). To build upon these baseline kinetic findings, future investigations could employ HPLC-based quantification targeting specific marker compounds of *P. laevigata* such as its characteristic proanthocyanidins alongside ex vivo skin permeation models to provide deeper insights into the biological penetration dynamics (Kamiya et al., 2001; Anggraini et al., 2022).

4. CONCLUSION

This study confirmed the successful characterization of *Parameria laevigata* bark extract and its integration into a PVA/PVP-based dissolving microneedle system for transdermal acne therapy, as evidenced by phytochemical screening, antioxidant assays, antibacterial evaluation, and physicochemical analyses. The extract exhibited strong antioxidant activity across DPPH, ABTS, and FRAP methods alongside moderate antibacterial activity against *Staphylococcus aureus* and *Cutibacterium acnes*, supporting a dual-action rationale addressing both microbial colonization and oxidative stress in acne pathogenesis. The optimized formulation (F2) demonstrated that a balanced PVA:PVP ratio was critical in determining morphological completeness, mechanical integrity sufficient for stratum corneum penetration, and extract–polymer compatibility confirmed by FTIR, with in vitro release following diffusion-controlled Korsmeyer–Peppas kinetics. These findings demonstrate that both coformer-in this context, polymer ratio-selection and bioactive source play critical roles in tuning the biological efficacy and structural performance of plant-based dissolving microneedle platforms. Overall, *P. laevigata* - loaded F2 arrays were identified as the most viable candidate for further development, underscoring the potential of Indonesian medicinal plant extracts as functional actives in transdermal DMN systems.

5. ACKNOWLEDGMENT

The authors would like to thank the Cosmetic Engineering Study Program, Sumatra Institute of Technology, for providing laboratory facilities during this research.

REFERENCES

Aisyah, A. N., M. Syawal, D. Ramadon, J. Djajadisastra, and R. Iswandana (2024). Formulation and Evaluation of Dissolving Microneedle for Transdermal Delivery of Piperine: The Effect of Polymers Concentration. *Journal of Biomaterials Science, Polymer Edition*, **35**(8); 1177–1196

Ali, R., P. Mehta, P. K. Monou, M. S. Arshad, E. Panteris, M. Rasekh, N. Singh, O. Qutachi, P. Wilson, D. Tzetzis, M. W. Chang, D. G. Fatouros, and Z. Ahmad (2020). Electrospinning/Electrospraying Coatings for Metal Microneedles: A Design of Experiments (DOE) and Quality by Design (QbD) Approach. *European Journal of Pharmaceutics and Biopharmaceutics*, **156**; 20–39

Alkhawaja, E., S. Hammadi, M. Abdelmalek, N. Mahasneh, B. Alkhawaja, and S. M. Abdelmalek (2020). Antibiotic Resistant *Cutibacterium acnes* among Acne Patients in Jordan: A Cross Sectional Study. *BMC Dermatology*, **20**(1); 17

Alrimawi, B. H., J. Y. Lee, K. W. Ng, and C. F. Goh (2024). In Vitro Evaluation of Microneedle Strength: A Comparison of Test Configurations and Experimental Insights. *RSC Pharmaceutics*, **1**(2); 227–233

Amano, N., Y. Takaki, H. Takei, M. Matsuo, M. Hara, Y. Tashiro, T. Oniki, T. Ito, and T. Hikima (2025). Fabrication and Mechanical/Biological Evaluations of Dissolving Bird-Bill Microneedle Arrays. *Drug Delivery and Translational Research*, **15**(7); 2581–2588

Anggraini, W., D. A. Purwanto, Isnaeni, and I. Kusumawati (2022). A Systematic Review of Potential Phytochemical Compound Bark of *Parameria laevigata* on Biofilm Formation. *International Journal of Applied Pharmaceutics*, **14**(Special Issue 1); 21–26

Anggraini, W., D. A. Purwanto, I. Kusumawati, and Isnaeni (2024). Mechanism and Antifungal Activities Vulvovaginal Candidiasis Isolated from Patients against Ethanol Extracts of *Parameria laevigata* (Juss.) Moldenke Stem Bark. *Pharmacognosy Journal*, **16**(3); 684–688

Arora, M. and T. T. Laskar (2023). Microneedles: Recent Advances and Development in the Field of Transdermal Drug Delivery Technology. *Journal of Drug Delivery and Therapeutics*, **13**(3); 155–163

Arya, P., D. Vaidya, M. Kaushal, S. Devi, A. Gupta, and S. Chand (2025). Effects of Different Solvents on Phytochemical Constituents, In-Vitro Antimicrobial Activity, and Volatile Components of *Boehmeria rugulosa* Wedd. Wood Extract. *Scientific Reports*, **15**(1); 29135

Atina, I. Royani, Assa'idah, and F. S. Arsyad (2025). Antibacterial Properties of Taro: Extraction, Antibacterial Testing Method, Modification and Application. *Science and Technology Indonesia*, **10**(2); 374–401

Balik, Z. B., A. R. Balık, E. F. Oğuz, Ö. Erel, and M. Tunca (2023). Evaluation of Thiol Disulfide Homeostasis and Ischemia-Modified Albumin Levels as an Indicator of Oxidative Stress in Acne Vulgaris. *Dermatology Practical and Conceptual*, **13**(4); e2023280

Balouiri, M., M. Sadiki, and S. K. Ibnsouda (2016). Methods for In Vitro Evaluating Antimicrobial Activity: A Review. *Journal of Pharmaceutical Analysis*, **6**(2); 71–79

Baskar, V., S. M. Meeran, A. Subbaraya, S. Sruthi, J. Ali, and T. Saravana Kumar (2018). Historic Review on Modern Herbal Nanogel Formulation and Delivery Methods. *International Journal of Pharmacy and Pharmaceutical Sciences*, **10**(10); 1–9

Bin Mokaizh, A. A., F. Tanjung, S. Almoughrabie, S. S. Dahham, S. Akter, and F. S. R. Al-Suede (2024). Ultrasonic-Assisted Extraction to Enhance the Recovery of Bioactive Phenolic Compounds From *Commiphora gileadensis* Leaves. *Ultrasonics Sonochemistry*, **103**; 106794

Bonfante, G., H. Lee, L. Bao, J. Park, N. Takama, and B. Kim

(2020). Comparison of Polymers to Enhance Mechanical Properties of Microneedles for Bio-Medical Applications. *Micro and Nano Systems Letters*, **8**(1); 13

Briuglia, M. L., A. J. Urquhart, and D. A. Lamprou (2014). Sustained and Controlled Release of Lipophilic Drugs From a Self-Assembling Amphiphilic Peptide Hydrogel. *International Journal of Pharmaceutics*, **474**(1–2); 103–111

Chaiwarit, T., B. Chanabodeechalermrung, P. Jantrawut, W. Ruksiriwanich, and M. Sainakham (2024). Fabrication and Characterization of Dissolving Microneedles Containing *Oryza sativa* L. Extract Complex for Enhancement of Transfollicular Delivery. *Polymers*, **16**(16); 2377

Chang, C.-C., M.-H. Yang, H.-M. Wen, and J.-C. Chern (2002). Estimation of Total Flavonoid Content in Propolis by Two Complementary Colorimetric Methods. *Journal of Food and Drug Analysis*, **10**(3); 178–182

Chaves, J. O., M. C. de Souza, L. C. da Silva, D. Lachos-Perez, P. C. Torres-Mayanga, A. P. d. F. Machado, T. Forster-Carneiro, M. Vázquez-Espinosa, A. V. González-de Peredo, G. F. Barbero, and M. A. Rostagno (2020). Extraction of Flavonoids From Natural Sources Using Modern Techniques. *Frontiers in Chemistry*, **8**; 507887

Ciobanu, C. S., L. Motelica, O. Oprea, M. D. Stelescu, D. Ficai, A. Ficai, and E. Andronescu (2023). Characterization of Tannin Extracts Derived from the Bark of Four Tree Species by HPLC and FTIR. *Journal of Forestry Research*, **34**(3); 821–836

Cordeiro, A. S., I. A. Tekko, M. H. Jomaa, L. Vora, E. McAlister, F. Volpe-Zanutto, M. Nethery, P. T. Baine, N. Mitchell, D. W. McNeill, and R. F. Donnelly (2020). Two-Photon Polymerisation 3D Printing of Microneedle Array Templates with Versatile Designs: Application in the Development of Polymeric Drug Delivery Systems. *Pharmaceutical Research*, **37**(9); 174

Davis, W. W. and T. R. Stout (1971). Disc Plate Method of Microbiological Antibiotic Assay. I. Factors Influencing Variability and Error. *Applied Microbiology*, **22**(4); 659–665

Demir, Y. K., Z. Akan, and O. Kerimoglu (2013). Characterization of Polymeric Microneedle Arrays for Transdermal Drug Delivery. *PLoS ONE*, **8**(10); e77289

Dontha, S. (2016). A Review on Antioxidant Methods. *Asian Journal of Pharmaceutical and Clinical Research*, **9**(Suppl. 2); 14–32

Economidou, S. N., M. J. Uddin, M. J. Marques, D. Douroumis, W. T. Sow, H. Li, A. Reid, J. F. C. Windmill, and A. Podoleanu (2021). A Novel 3D Printed Hollow Microneedle Microelectromechanical System for Controlled, Personalized Transdermal Drug Delivery. *Additive Manufacturing*, **38**; 101815

Fitaihi, R., S. Abukhamees, S. H. Chung, and D. Q. M. Craig (2024). Optimization of Stereolithography 3D Printing of Microneedle Micro-Molds for Ocular Drug Delivery. *International Journal of Pharmaceutics*, **658**; 124195

Hanisah, A., K. Omar, and S. A. Shah (2009). Prevalence of Acne and Its Impact on the Quality of Life in School-Aged Adolescents in Malaysia. *Journal of Primary Health Care*, **1**(1); 20–25

Hashempur, M. H., F. Ghorat, F. Karami, A. Jahanbin, H. Nouraei, M. Abbasi, M. Jafari, A. Zare, S. Barzegar, and Z. Zareshahrabadi (2025). Topical Delivery Systems for Plant-Derived Antimicrobial Agents: A Review of Current Advances. *International Journal of Biomaterials*, **2025**(1); 4251091

Jiang, F. and D. Drummer (2022). Analysis of UV Curing Strategy on Reaction Heat Control and Part Accuracy for Additive Manufacturing. *Polymers*, **14**(4); 759

J.R., S. D. Jothi, and V. Raghavan (2022). Oxidative Stress in Acne Vulgaris. *International Journal of Pharmacy and Pharmaceutical Sciences*, **14**(9); 41–44

Justyna, K., S. Patrycja, M. Krzysztof, and W. Rafal (2025). Dissolving Microneedles Fabricated from 3D-Printed Master Molds for Application in Veterinary Medicine. *Scientific Reports*, **15**(1); 14102

Kamiya, K., C. Watanabe, H. Endang, M. Umar, and T. Satake (2001). Studies on the Constituents of Bark of *Parameria laevigata* Moldenke. *Chemical and Pharmaceutical Bulletin*, **49**(5); 551–557

Kurakula, M. and G. S. N. K. Rao (2020). Pharmaceutical Assessment of Polyvinylpyrrolidone (PVP): As Excipient from Conventional to Controlled Delivery Systems with a Spotlight on COVID-19 Inhibition. *Journal of Drug Delivery Science and Technology*, **60**; 101581

Lee, I. C., Y. C. Wu, S. W. Tsai, C. H. Chen, and M. H. Wu (2017). Fabrication of Two-Layer Dissolving Polyvinylpyrrolidone Microneedles with Different Molecular Weights for In Vivo Insulin Transdermal Delivery. *RSC Advances*, **7**(9); 5067–5075

Legiawati, L., P. A. Halim, M. Fitriani, H. G. Hikmahrachim, and H. W. Lim (2023). Microbiomes in Acne Vulgaris and Their Susceptibility to Antibiotics in Indonesia: A Systematic Review and Meta-Analysis. *Antibiotics*, **12**(1); 145

Li, Y., X. Hu, G. Dong, X. Wang, and T. Liu (2024). Acne Treatment: Research Progress and New Perspectives. *Frontiers in Medicine*, **11**; 1425675

Lundborg, M., C. L. Wennberg, A. Narangifard, E. Lindahl, and L. Norlén (2018). Predicting Drug Permeability through Skin Using Molecular Dynamics Simulation. *Journal of Controlled Release*, **283**; 269–279

Luo, L., G. Li, D. Luan, Q. Yuan, Y. Wei, and X. Wang (2019). Low-Cost Ru/C-Catalyzed Depolymerization of the Polymeric Proanthocyanidin-Rich Fraction from Bark to Produce Oligomeric Proanthocyanidins with Antioxidant Activity. *ACS Omega*, **4**(21); 19393–19401

Luo, X., L. Yang, and Y. Cui (2023). Microneedles: Materials, Fabrication, and Biomedical Applications. *Biomedical Microdevices*, **25**(3); 20

Makvandi, P., M. Kirkby, A. R. J. Hutton, M. Shabani, C. K. Y. Yiu, Z. Baghbantaraghdari, R. Jamaledin, M. Carlotti, B. Mazzolai, V. Mattoli, and R. F. Donnelly (2021). Engineering Microneedle Patches for Improved Penetra-

tion: Analysis, Skin Models and Factors Affecting Needle Insertion. *Nano-Micro Letters*, **13**(1); 93

Mawu, F. O., A. G. H. Rompis, G. M. Kapantow, and S. H. R. Ticoalu (2025). The Efficacy of Combination of Oral Antioxidants and Topical Retinoic Acid versus Topical Retinoic Acid Monotherapy in Mild Acne Vulgaris Patients. *Indonesian Journal of Biomedicine and Clinical Sciences*, **6**(1); 23–30

Mohammadi, H., A. Ebrahimian, and N. Maftoon (2021). Fracture Behaviour of Human Skin in Deep Needle Insertion Can Be Captured Using Validated Cohesive Zone Finite-Element Method. *Computers in Biology and Medicine*, **139**; 104982

More, P. R. and S. S. Arya (2021). Intensification of Bio-Actives Extraction from Pomegranate Peel Using Pulsed Ultrasound: Effect of Factors, Correlation, Optimization and Antioxidant Bioactivities. *Ultrasonics Sonochemistry*, **72**; 105423

Muharrami, L. K., F. Munawaroh, T. Ersam, and M. Santoso (2020). Phytochemical Screening of Ethanolic Extract: A Preliminary Test on Five Medicinal Plants on Bangkalan. *Jurnal Pena Sains*, **7**(2); 96–102

Ning, X., C. Wiraja, D. C. S. Lio, and C. Xu (2021). Transdermal Delivery of Chinese Herbal Medicine Extract Using Dissolvable Microneedles for Hypertrophic Scar Treatment. *Acta Pharmaceutica Sinica B*, **11**(11); 3610–3619

Oh, N. G., Y. J. Son, M. J. Choi, G. Chun, M. D. Truong, S. E. Shin, and H. S. Yoo (2022). Fabrication of a PVA-Based Hydrogel Microneedle Patch. *ACS Omega*, **7**(18); 15576–15585

Oliveira, C., J. A. Teixeira, N. Oliveira, S. Ferreira, and C. M. Botelho (2024). Microneedles' Device: Design, Fabrication, and Applications. *Macromol*, **4**(2); 320–355

Onesto, V., C. Di Natale, M. Profeta, P. A. Netti, and R. Vecchione (2020). Engineered PLGA-PVP/VA Based Formulations to Produce Electro-Drawn Fast Biodegradable Microneedles for Labile Biomolecule Delivery. *Progress in Biomaterials*, **9**(4); 203–217

Popa, G. L., C. I. Mitran, M. I. Mitran, M. Tampa, C. Matei, M. I. Popa, and S. R. Georgescu (2023). Markers of Oxidative Stress in Patients with Acne: A Literature Review. *Life*, **13**(7); 1433

Rabiei, M., S. Kashanian, G. Bahrami, H. Derakhshankhah, E. Barzegari, S. S. Samavati, and S. J. P. McInnes (2021). Dissolving Microneedle-Assisted Long-Acting Liraglutide Delivery to Control Type 2 Diabetes and Obesity. *European Journal of Pharmaceutical Sciences*, **167**; 106040

Rimadhani, M. and Rahmadewi (2015). Pengaruh Hormon terhadap Akne Vulgaris. *Berkala Ilmu Kesehatan Kulit dan Kelamin*, **27**(3); 218–224. In Indonesian

Ruchiatan, K., T. Rizqandaru, P. R. Satjamanggala, N. Tache, A. I. Cahyadi, A. Rezano, H. Gunawan, E. K. Sutedja, R. F. Dwiyana, R. M. N. Hidayah, P. A. Achdiat, E. Sutedja, O. Suwarsa, and R. Hindritiani (2023). Characteristics of Biofilm-Forming Ability and Antibiotic Resistance of *Cutibacterium acnes* and *Staphylococcus epidermidis* from Acne Vulgaris Patients. *Clinical, Cosmetic and Investigational Dermatology*, **16**; 2457–2465

Saludarez, M. (2019). Anti-Bacterial and Anti-Inflammatory Property Evaluation of *Parameria laevigata* (Lupiit) for the Formulation of an Ointment. *International Journal of Advanced Research*, **7**(6); 488–496

Santos-Sánchez, N. F., R. Salas-Coronado, C. Villanueva-Cañongo, and B. Hernández-Carlos (2019). Antioxidant Compounds and Their Antioxidant Mechanism. In *Antioxidants*. IntechOpen

Saragih, D. F., H. Opod, and C. Pali (2016). Hubungan Tingkat Kepercayaan Diri dan Jerawat (*Acne vulgaris*) pada Siswa-Siswi Kelas XII di SMA Negeri 1 Manado. *eBiomedik*, **4**(1). In Indonesian

Seetharam, A. A., M. G. Shivananjegowda, K. Bangarurajan, and D. V. Gowda (2024). Evaluation of the Feasibility of Transdermal Delivery of Neratinib (NB) Loaded Microneedles to Treat Breast Cancer. *Indian Journal of Pharmaceutical Education and Research*, **58**(2S); S403–S411

Shimamoto, Y., S. Matsushita, T. Yamamoto, Y. Nakamura, A. Kamada, M. Miyata, and K. Umimoto (2019). Real-Time Measurement of Polyvinylpyrrolidone Eluted from Polysulfone Membrane Dialyzers Based on the Ultraviolet Spectrum. *ASAIO Journal*, **65**(5); 522–526

Siddiqui, I., U. Rais, and M. Tahir (2024). Exploring Stress-Induced Mechanisms in Acne Pathogenesis

Tai, M., C. Zhang, Y. Ma, J. Yang, Z. Mai, C. Li, and G. Leng (2022). Acne and Its Post-Inflammatory Hyperpigmentation Treatment by Applying Anti-Acne Dissolving Microneedle Patches. *Journal of Cosmetic Dermatology*, **21**(12); 6913–6919

Teodorescu, M., M. Bercea, and S. Morariu (2019). Biomaterials of PVA and PVP in Medical and Pharmaceutical Applications: Perspectives and Challenges. *Biotechnology Advances*, **37**(1); 109–131

Tijani, A., P. Dogra, M. J. Peláez, Z. Wang, V. Cristini, and A. Puri (2023). Mechanistic Modeling-Guided Optimization of Microneedle-Based Skin Patch for Rapid Transdermal Delivery of Naloxone for Opioid Overdose Treatment. *Drug Delivery and Translational Research*, **13**(1); 320–338

Tsuboko, Y., H. Sakoda, Y. Okamoto, Y. Nomura, and E. Yamamoto (2024). Mechanical Characterization of Individual Needles in Microneedle Arrays: Factors Affecting Compression Test Results. *Pharmaceutics*, **16**(11); 1480

Utami, Y. P., R. Yulianty, Y. Y. Djabir, and G. Alam (2024). Antioxidant Activity, Total Phenolic and Total Flavonoid Contents of *Etlingera elatior* (Jack) R.M. Smith from North Luwu, Indonesia. *Tropical Journal of Natural Product Research*, **8**(1); 5955–5961

Wang, Q., J. Jiang, W. Chen, H. Jiang, Z. Zhang, and X. Sun (2024). Dissolving Hyaluronic Acid-Based Microneedles to Transdermally Deliver Eugenol Combined with Photothermal Therapy for *Acne vulgaris* Treatment. *ACS Applied Materials & Interfaces*, **16**(17); 21595–21609

Wang, Y., Z. Deng, X. Wang, Y. Shi, Y. Lu, S. Fang, and X. Liang (2021). Formononetin/Methyl-β-Cyclodextrin

Inclusion Complex Incorporated into Electrospun Polyvinyl-Alcohol Nanofibers: Enhanced Water Solubility and Oral Fast-Dissolving Property. *International Journal of Pharmaceutics*, **603**; 120696

Wiadnyani, K. A., A. Dharmayudha, L. M. Sudimartini, and I. M. Merdana (2024). Identification of Chemical Compounds Ethanol Extract Leaf Mimosa That Grows in Denpasar City. *Buletin Veteriner Udayana*, **16**(1); 64–72

Wu, X. R., B. Y. Tan, H. B. Ye, F. R. Liu, H. Z. Peng, M. Xia, X. H. Wang, X. M. Shen, M. J. Yang, X. M. Liu, Y. L. Zhao, and X. D. Luo (2025). *Parameria laevigata* (Juss.) Moldenke Healing Wound via PI3K/AKT/MAPK Pathway. *Journal of Ethnopharmacology*, **360**; 121148

Yan, Y., X. Li, C. Zhang, L. Lv, B. Gao, and M. Li (2021). Research Progress on Antibacterial Activities and Mechanisms of Natural Alkaloids: A Review. *Antibiotics*, **10**(3); 318

Yang, B., Y. Dong, Y. Shen, A. Hou, G. Quan, X. Pan, and C. Wu (2021). Bilayer Dissolving Microneedle Array Containing 5-Fluorouracil and Triamcinolone with Biphasic Release Profile for Hypertrophic Scar Therapy. *Bioactive Materials*, **6**(8); 2400–2411

Yazdani, S., M. Mozaffarian, G. Pazuki, N. Hadidi, I. Gallego, G. Puras, and J. L. Pedraz (2022). Design of Double Functionalized Carbon Nanotube for Amphotericin B and Genetic Material Delivery. *Scientific Reports*, **12**(1); 21114

Zhang, J., P. Guo, M. Qiu, G. Zhong, Q. Yang, P. Lei, K. Gou, R. Zeng, C. Zhang, and Y. Qu (2024). A Novel Natural Polysaccharide Dissolving Microneedle Capable of Adsorbing Pus to Load EGCG for the Treatment of *Acne vulgaris*. *Materials and Design*, **238**; 112639

Zhang, Y., Y. Shang, J. Bao, and Y. Wang (2025). Molecular Pathogenesis of Acne and Their Microneedle Treatments. *Engineered Regeneration*, **6**; 235–248

Zhu, Z., X. Zhong, Z. Luo, M. Liu, H. Zhang, H. Zheng, and J. Li (2025). Global, Regional and National Burdens of *Acne vulgaris* in Adolescents and Young Adults Aged 10–24 Years from 1990 to 2021: A Trend Analysis. *British Journal of Dermatology*, **192**(2); 228–237

